



Boosting ultrafast Li storage kinetics of conductive Nb-doped TiO₂ functional layer coated on LiMn₂O₄

Ki-Wook Sung^a, Dong-Yo Shin^b, Hyo-Jin Ahn^{a,b,*}

^a Department of Materials Science and Engineering, Seoul National University of Science and Technology, Seoul 01811, South Korea

^b Program of Materials Science & Engineering, Convergence Institute of Biomedical Engineering and Biomaterials, Seoul National University of Science and Technology, Seoul 01811, South Korea



ARTICLE INFO

Article history:

Received 9 December 2020
Received in revised form 6 February 2021
Accepted 28 February 2021
Available online 4 March 2021

Keywords:

Lithium-ion batteries
Lithium manganese oxide
Nb-doped TiO₂
Interfacial coating layer
Ultrafast Li storage kinetics

ABSTRACT

Interface engineering of LiMn₂O₄ (LMO) is a promising strategy to enhance the lithium storage capability and cycling stability of cathode materials in Li-ion batteries (LIBs). This is because the strategy prevents structural degradation; however, Li storage kinetics remains unsatisfactory, resulting in poor ultrafast cycling performance. Therefore, we fabricated an Nb-doped TiO₂ (NTO) functional layer as a conductive passivation layer on the LMO surface by horizontal ultrasonic spray pyrolysis deposition. The NTO functional layer suppressed the volume expansion of LMO and exhibited high electrical and ionic conductivity, which resulted in improved structural stability of LMO (related to cycling stability) and increased electron/ion transfer rate (related to ultrafast cycling performance). In the TiO₂ structure, Ti⁴⁺ ions were replaced by Nb⁵⁺ ions, which possess high electrical conductivity and a wide c-axis as a Li-ion diffusion route. As a result, the NTO-coated LMO cathode material showed an outstanding specific capacity of 112.7 mAh/g with a remarkable capacity retention of 96.2% after 100 cycles at a current density of 1 C and excellent ultrafast cycling capacity and stability of 70.0 mAh/g after 500 cycles at a current density of 10 C.

© 2021 Elsevier B.V. All rights reserved.

1. Introduction

In recent years, global issues such as the exhaustion of fossil fuels, global warming, and environmental pollution have triggered an interest in the development of eco-friendly energy storage devices [1]. Among various energy storage devices, Li-ion batteries (LIBs) have been used extensively as power source for portable devices, such as laptops and smartphones, owing to their good cycling stability, high energy density, low self-discharge rate, little memory effect, and environmental friendliness [2–4]. However, LIBs exhibit slow charging time and short mileage, resulting in poor performance [5,6].

The cathode material in LIBs is one of the key components that can improve the electrochemical performance of LIBs, in terms of energy density, lifetime, and charging speed [7]. Among various cathode materials, spinel lithium manganese oxide (LiMn₂O₄, LMO) has received considerable attention owing to its advantages of high theoretical capacity (148 mAh/g), high power density, high operating

voltage (3.5–4.5 V), cost-effectiveness, and non-toxicity [8,9]. However, the applications of LMO are limited because of three main problems: (1) Mn dissolution by Jahn–Teller distortion, (2) low Li-ion diffusion rate, and (3) low electrical conductivity [10–12]. To overcome these problems, strategies such as morphology control, cation doping, and surface coating have been developed to enhance the Li-ion storage performance, i.e., increasing the cycling stability of LMO [13–15]. In particular, interface engineering by fabricating protecting layers (e.g., CeO₂, ZnO, Al₂O₃, and MoO₃) on LMO is a potential strategy to enhance the structural/electrochemical stability of LMO by suppressing the volume expansion and preventing Mn dissolution or promoting Li-ion and electron diffusion of the LMO during charging/discharging processes [13–17]. Although previously reported surface coatings made of metal oxides material showed improved cycling stability at a low current density, they showed low specific capacity and cycling stability under ultrafast cycling conditions owing to the limited electron and Li-ion diffusion rate due to the high electrical/ionic resistance of the metal oxide coating layer. Thus, a novel interfacial layer with having high electrical/ionic conductivity that can effectively prevent the Jahn–Teller distortion and Mn dissolution should be developed to achieve fast Li-ion storage kinetics.

* Corresponding author at: Department of Materials Science and Engineering, Seoul National University of Science and Technology, Seoul 01811, South Korea.

E-mail address: hjahn@seoultech.ac.kr (H.-J. Ahn).

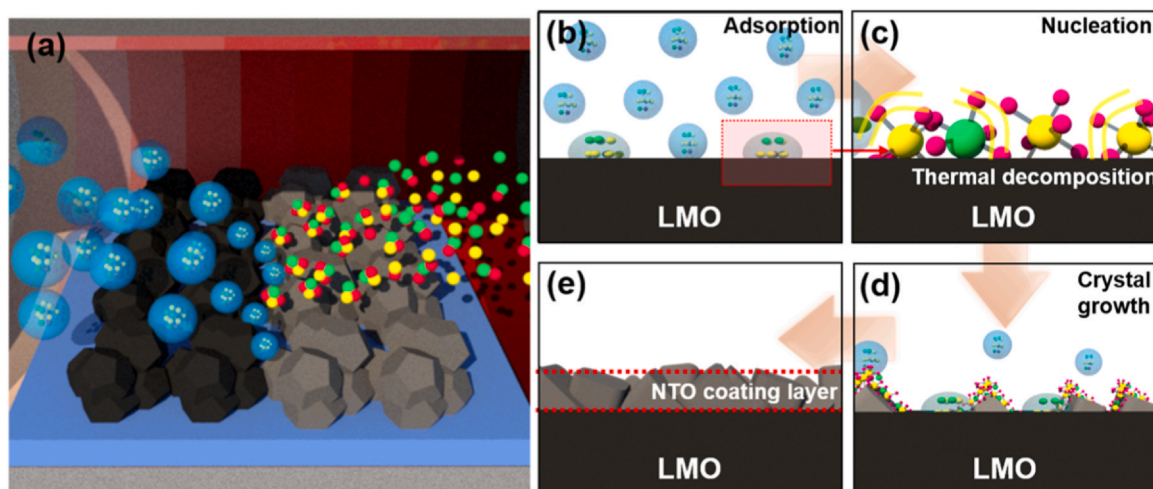


Fig. 1. Schematic illustration of formation mechanism for conductive NTO coating layer on surface of LMO using HUSPD.

In this study, we propose a novel structure of a conductive Nb-doped TiO_2 (NTO) functional layer coated on the surface of LMO using horizontal ultrasonic spray pyrolysis deposition (HUSPD) to boost the electrochemical kinetics of LMO such that it can be used in ultrafast LIBs. HUSPD is a solution-based deposition process; it is simpler and more cost-effective compared to other vacuum-based deposition processes (such as atomic layer deposition, chemical vapor deposition, and magnetron sputtering). Furthermore, the NTO functional layer has higher electrical conductivity (10^{-10} – 10^{-5} S/cm) and Li-ion conductivity than those of the TiO_2 interfacial layer (10^{-15} – 10^{-9} cm^2/s), leading to outstanding Li-ion storage kinetics [18,19].

2. Experimental

The conductive NTO functional layer on the surface of LMO was synthesized using HUSPD. First, the 15% titanium diisopropoxide ($\text{C}_{16}\text{H}_{28}\text{O}_6\text{Ti}$, Alfa Aesar) and niobium chloride (NbCl_5 , Sigma) were dissolved in ethanol, and whereby the mole ratio of Nb/Ti was fixed at 5. The precursor solution was sprayed onto the LMO (metal impurity <25 ppb, POSCO M-TECH) using an ultrasonic atomizer (1.6 MHz). The temperature and stage rotation speed in the reaction chamber were maintained at 400 °C and 5 rpm, respectively. The flow rate of the air carrier gas was fixed at 15 L/min. To optimize the NTO interfacial layer on the LMO surface, the deposition time was controlled at 0, 20, 40, and 60 min (herein designated as bare LMO, NTO-LMO20, NTO-LMO40, and NTO-LMO60, respectively). Also, to clearly investigate crystal structure of the NTO, the NTO was coated on cleaned Si wafer without LMO with different deposition times of 40, 80, 120 min, which were named as NTO40, NTO80, and NTO120.

The morphologies were examined using field-emission scanning electron microscopy (FESEM), transmission electron microscopy (TEM), and energy-dispersive X-ray spectroscopy (EDS) mapping. The crystal structures and chemical bonding states were investigated using X-ray diffraction (XRD) and X-ray photoelectron spectroscopy (XPS). Electrical conductivities were determined using Hall effect measurements.

The electrochemical performance was verified using coin-type cells (CR2032, Hohsen Corporation), which are composed of prepared samples as the cathode, a Li foil (Honjo Chemical, 99.99%) as the anode, a porous polypropylene membrane as the separator, and a 1.6 M LiPF_6 solution dissolved in a mixture of ethylene carbonate and dimethyl carbonate (1:1) as the electrolyte. To fabricate the cathode electrode, slurries were prepared by mixing 70 wt% samples as the active material, 10 wt% Ketjen black as the conductive

material, and 20 wt% polyvinylidene fluoride (PVDF, Sigma) as a binder in N-methyl-2-pyrrolidinone (NMP, Sigma). The slurries were coated on an Al foil and dried at 100 °C for 10 h. All coin-type cells were assembled in a high-purity argon-filled glove box maintaining the concentration of H_2O and O_2 less than 5 ppm. Electrochemical impedance spectroscopy (EIS) was performed in the frequency range of 10^5 – 10^{-2} Hz. The electrochemical performance was investigated using a battery cycler (WonATech Corp., WMPG 3000S) in from the potential range of 3.3–4.3 V (vs. Li/Li^+). Cycling stability tests were performed for up to 100 cycles at 1 C (180 mA/g). The rate performance was evaluated at current densities of 1, 3, 5, 7, and 10 C. The ultrafast cycling performance was observed at 10 C for 500 cycles. To confirm the Nb doping effect, pure TiO_2 -coated LMO was also fabricated, and rate performance was evaluated. Also, to confirm the effect of preventing Mn dissolution of conductive NTO functional layer, the FESEM and EDS analyses of bare LMO and NTO-LMO40 after 500 cycles at 10 C were conducted, and cyclic voltammetry of bare LMO and NTO-LMO electrode was conducted at 1 mV/s during 50 cycles.

3. Results and discussion

Fig. 1 shows a schematic of the HUSPD process and the formation steps of the conductive NTO functional layer on the surface of LMO. The precursor solution was horizontally supplied on the LMO surface placed in a reaction chamber by with ($\text{O}_2:\text{N}_2 = 20:80$) as the carrier gas. First, the droplets of precursors of Nb, Ti, and O were formed by ultrasonication and horizontally transferred to the LMO surface (Fig. 1b). Then, the N-doped TiO_2 nucleated on the surface of LMO by following formation steps: (1) adsorption of droplets, (2) solvent evaporation, (3) solute condensation, and (4) thermal decomposition [20]. At the initial time of deposition, the nucleus of NTO was formed on the LMO surface (Fig. 1c). As the deposition time was increased, NTO nanoparticles were crystallized and formed by the continued supply of homogeneous droplets (Fig. 1d). Then, the NTO particles were grown and stacked on the LMO surface, resulting in the formation of dense and thin layer structures of NTO on the LMO surface (Fig. 1e) [21]. Therefore, the conductive NTO functional layer coated on the surface of LMO can perform as a stable protecting layer and can allow efficient electron/ion transfer, leading to improved ultrafast Li-ion storage kinetics.

The morphology of the conductive NTO functional layer in all samples was analyzed by FESEM. The low-magnification FESEM images (Fig. 2a–d) of bare LMO, NTO-LMO20, NTO-LMO40, and NTO-LMO60 indicate the aggregation of secondary particles with

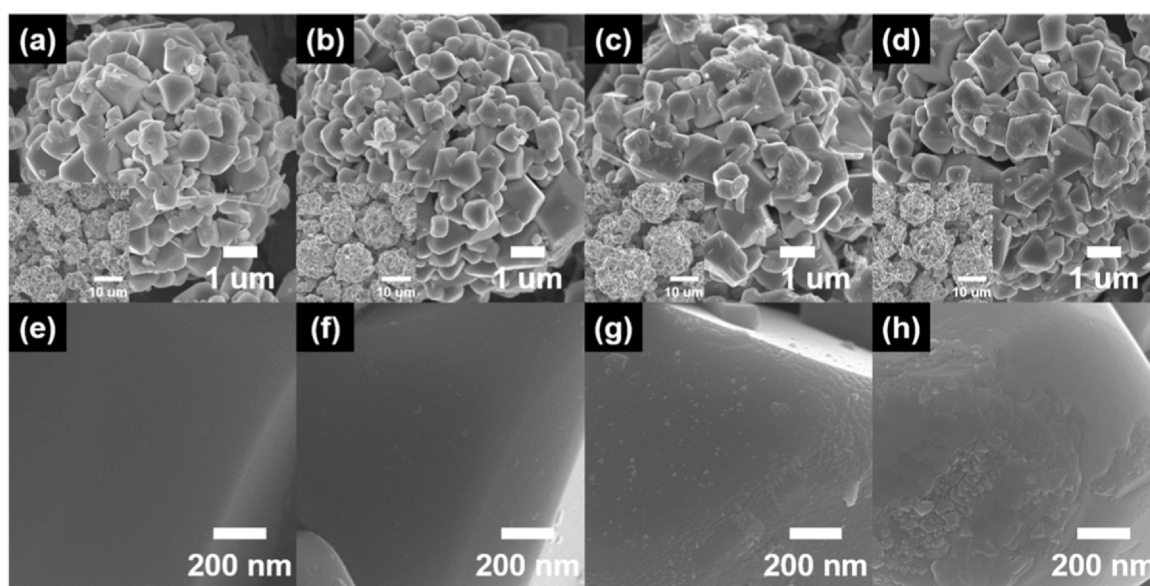


Fig. 2. (a–d) Low-magnification and (e–h) high-magnification FESEM images of Bare LMO, NTO-LMO20, NTO-LMO40, and NTO-LMO60.

diameters of 7.6–8.4 μm , which are composed of primary particles diameters with diameter of 466.7–752.8 nm. However, as seen in high-magnification FESEM images (Fig. 2e–h), bare LMO showed a smooth surface the morphology on primary particles (Fig. 2e), and NTO-LMO20 and NTO-LMO40 showed a rough surface with the presence of nanoparticles, which indicates the formation of NTO nanoparticles with diameters of 15.7–24.0 nm and 20.6–32.1 nm, respectively (Fig. 2f and g). The droplets adsorbed on the LMO surface could formed island-type NTO nanoparticles, and a thin NTO interfacial layer uniformly formed as the deposition time increased. However, after a long deposition duration, NTO-LMO60 exhibited a thick interfacial layer and agglomerated NTO nanoparticles with a diameter of 34.8–66.0 nm (Fig. 2h). The conductive NTO functional layer of NTO-LMO40 was a thin and dense interfacial layer and could act as an efficient protective layer that suppresses the volume expansion and Mn dissolution of the LMO.

To further examine the structures of the conductive NTO functional layers coated on the surface of LMO surfaces, TEM analysis

was performed, as shown in Fig. 3a–d. Low-magnification TEM images show that bare LMO showed a smooth surface (Fig. 3a), whereas a coated layer structure was observed on NTO-LMO40 (Fig. 3b). The thickness of the uniform NTO coating layer of NTO-LMO40 was 18.1–20.3 nm uniformly. In addition, as seen in the high-magnification TEM image of NTO-LMO40 (Fig. 3c), the interlayer distance of NTO (0.36 nm) is higher than that of TiO_2 (0.35 nm) because of the higher ionic radius of Nb^{5+} ions (6.4 nm) that substitute Ti^{4+} ions (6.1 nm) in the TiO_2 structure [22,23]. In general, doped Nb atoms increase the lattice parameter of the c-axis in rutile TiO_2 by a large ionic radius of Nb^{5+} , which can improve the Li-ion diffusion rate by, as shown in Fig. S1 [18]. Furthermore, the TEM-EDS mapping result of NTO-LMO40 shows well-dispersed Mn, O, Ti, and Nb in the NTO functional layer (Fig. 1h). Therefore, this novel conductive NTO functional layer on the LMO surface can act as a passivation layer to prevent Mn dissolution and the conductive layer related to the Li-ion transfer route, effectively improving the cycling stability and ultra-fast cycling performance.

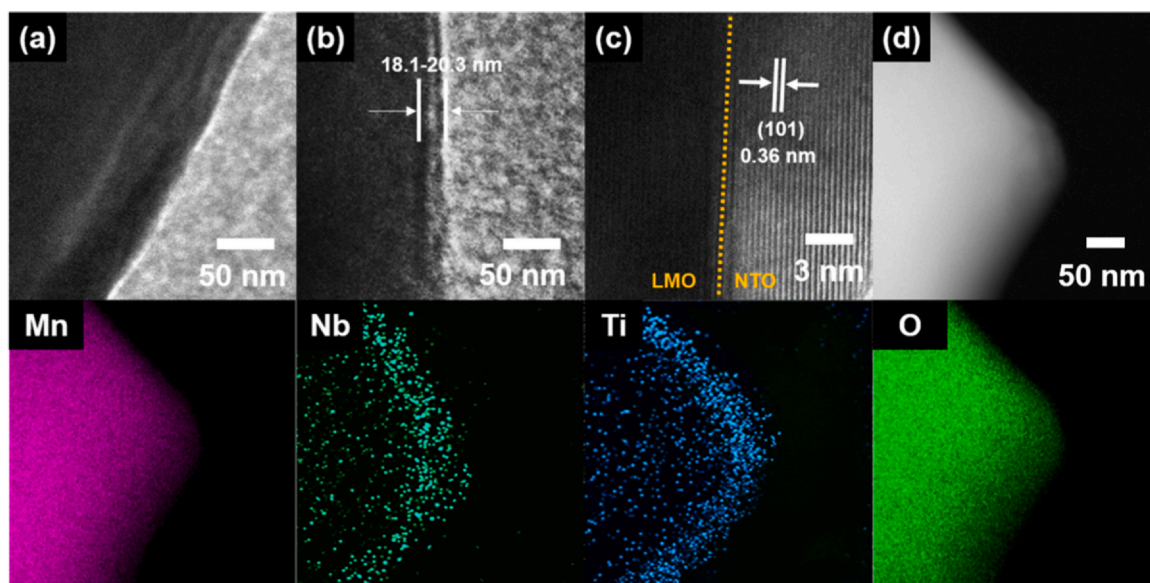


Fig. 3. (a, b) Low-magnification TEM images of Bare LMO and NTO-LMO20, (c) high-magnification TEM image and TEM-EDS mapping data of NTO-LMO40.

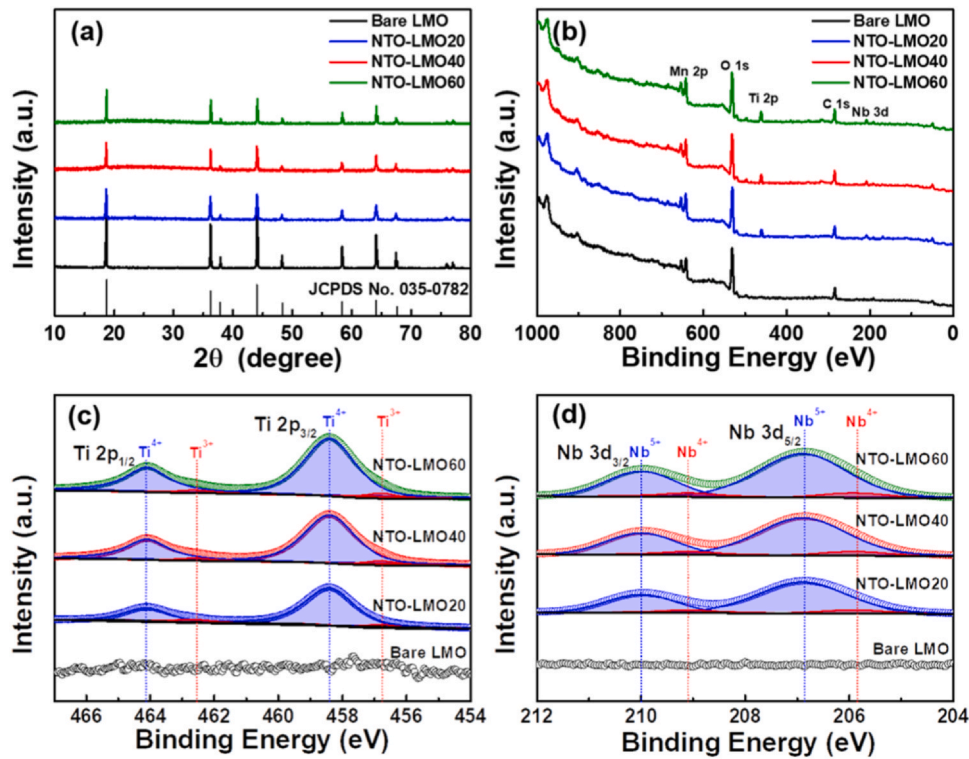


Fig. 4. (a) XRD patterns, (b) XPS full scan spectrum, and XPS spectra obtain from (c) Ti 2p and (d) Nb 3d of bare LMO, NTO-LMO20, NTO-LMO40, and NTO-LMO60.

Fig. 4a shows the XRD patterns of all samples. All samples showed diffraction peaks at 18.7° , 36.2° , 43.9° , and 63.9° , corresponding to the (111), (311), (400), and (440) planes, respectively, of the spinel LMO phase (JCPDS card No. 035-0782). Due to the thin NTO interfacial layer of 18.1–20.3 nm compared to the bulk LMO, the diffraction peaks of the NTO phase are not clearly observed [21,24]. In this connection, to clearly investigate crystal structure of the conductive NTO functional layer, Fig. S1 displays the XRD patterns of NTO40, NTO80, and NTO120. All samples showed diffraction peaks at $\sim 27.4^\circ$ corresponding to the (110) plane of a rutile NTO phase (space group of $P4_2/mnm$ [136], JCPDS card no. 21-1276), which is observed shift toward low angle by larger ionic radius of doped Nb^{5+} (6.4 nm) than Ti^{4+} (6.1 nm). This result implies that the NTO functional layer exhibits a rutile structure.

To investigate the chemical bonding states of all samples, XPS analysis was performed (Fig. 2b–d). In the full scan spectrum of the NTO-LMO samples, Mn 2p, O 1s, Ti 2p, and Nb 3d peaks were clearly observed without other impurity phases (Fig. 2b). The Ti 2p spectrum of the NTO-LMO samples showed two major peaks at 458.4 eV for $2p_{3/2}$ and 464.1 eV for $2p_{1/2}$, indicating the Ti^{4+} state was present in the TiO_2 phase (blue area). In addition, two minor peaks at 456.7 eV for $2p_{3/2}$ and 462.5 eV for $2p_{1/2}$ were observed, indicating the Ti^{3+} state (red area), which is formed by Nb^{5+} ions replacing in the Ti^{4+} in NTO phase (Fig. 2c). In addition, for the Nb 3d XPS spectra of all samples (Fig. 3d), major peaks were observed at 206.6 eV for Nb $3d_{5/2}$ and 210.0 eV for Nb $3d_{3/2}$, as well as minor peaks at 205.8 eV for Nb $3d_{5/2}$ and 209.1 eV for Nb $3d_{3/2}$, corresponding to the Nb^{5+} and Nb^{4+} states, respectively [25–28]. The presence of Nb^{5+} and Nb^{4+} ions confirmed the doping of the doped Nb ions in the TiO_2 structure and the binding of oxidized Nb ions to oxygen outside the NTO lattice [25,27,28].

To confirm the electrochemical kinetics of the conductive NTO coating layer on the LMO surface, EIS analysis of all samples was performed. The Nyquist plot is composed of semicircles in the high-frequency region, which indicate the charge transfer resistance (R_{ct}) at the electrode/electrolyte interface, and an inclined line in the low-

frequency region, indicating Li-ion diffusion resistance (called Warburg impedance) [29,30]. As expected, the NTO-LMO40 electrode showed the smallest lowest R_{ct} and low Warburg impedance, thus providing a high electrical/ionic transfer rate (Fig. 5a, b). Furthermore, the Li-ion diffusion coefficients of all samples were calculated using Eqs. (1) and (2) [29,30].

$$Z_{real} = R_e + R_{ct} + \sigma_w \omega^{-1/2} \quad (1)$$

$$D = R^2 T^2 / 2A^2 n^4 F^4 C^2 \sigma_w \quad (2)$$

where σ_w , D , R , T , F , and C are the Warburg impedance coefficient, Li-ion diffusion coefficient, gas constant, temperature, Faraday's constant, and molar concentration, respectively. The Li-ion diffusion coefficient of the NTO-LMO40 electrode was the highest, $14.3 \times 10^{-13} \text{ cm}^2 \text{ s}^{-1}$, compared to those of other samples ($9.1 \times 10^{-13} \text{ cm}^2 \text{ s}^{-1}$ for bare LMO, $10.5 \times 10^{-13} \text{ cm}^2 \text{ s}^{-1}$ for NTO-LMO20, and $12.1 \times 10^{-13} \text{ cm}^2 \text{ s}^{-1}$ for NTO-LMO60, as shown in Fig. 5c). The thickness of the conductive NTO interfacial layer in NTO-LMO40 was optimum, which led to reduced Li-ion diffusion resistance. Moreover, the electrical conductivities of all electrodes were investigated using Hall effect measurements, as shown in Fig. 5d. NTO-LMO40 ($1.41 \times 10^2 \text{ S cm}^{-1}$) and NTO-LMO60 ($1.45 \times 10^2 \text{ S cm}^{-1}$) exhibited significantly higher electrical conductivities compared to those of bare LMO ($0.90 \times 10^2 \text{ S cm}^{-1}$) and NTO-LMO20 ($1.07 \times 10^2 \text{ S cm}^{-1}$) owing to the well-formed conductive NTO interfacial layer on the LMO surface. Therefore, the optimized NTO functional layer coated on the LMO surface can effectively boost increase the ultrafast Li storage performance by fast electron/ion transfer kinetics.

Fig. 6a displays the charge/discharge test of all electrodes at 1 C for during 100 cycles. The bare LMO electrode exhibited indicated a low specific capacity of 92.5 mAh/g with a poor capacity retention of 84.7%, owing to structural degradation caused by volume expansion and Mn dissolution. However, NTO coated on LMO electrodes showed improved cycling stability compared to that of the bare LMO electrode. Among them, NTO-LMO40 showed the highest

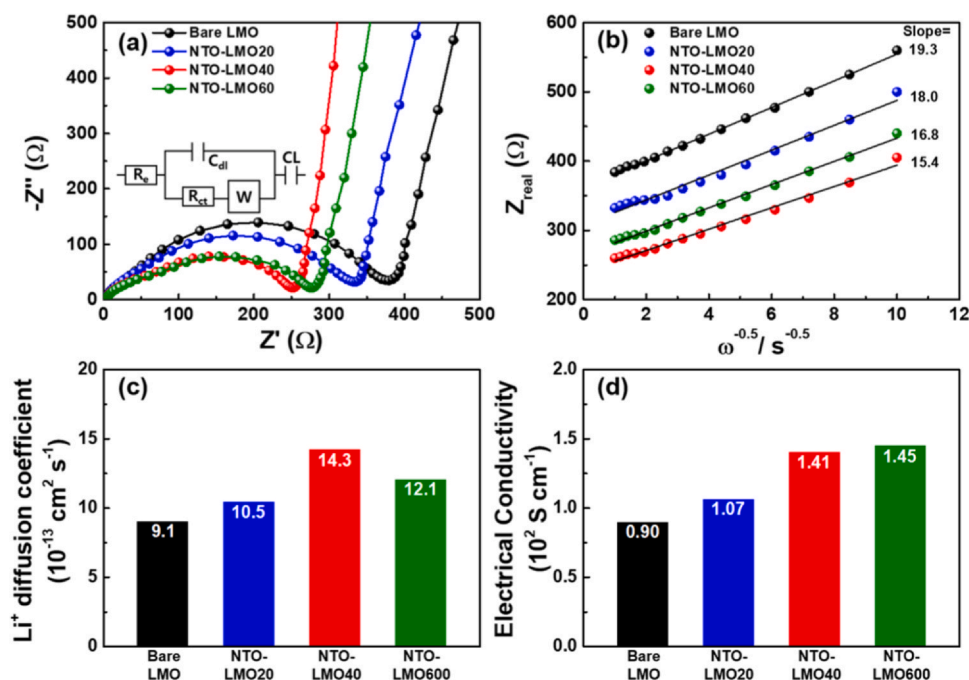


Fig. 5. (a) Nyquist plots, (b) relationship between Z_{real} and $\omega^{-1/2}$ in the low frequency region, Li^+ diffusion coefficient, and Electrical conductivity of bare LMO, NTO-LMO20, NTO-LMO40, and NTO-LMO60.

specific capacity of 112.7 mAh/g with a superior capacity retention of 96.2% after 100 cycles compared to those of NTO-LMO20 (100.1 mAh/g with 89.6% retention) and NTO-LMO60 (112.7 mAh/g with 90.9% retention) owing to the optimized NTO coating layer. This result suggests that the cycling stability of LMO is primarily ascribed to the effective prevention of Mn dissolution and suppression of volume expansion. In addition, the C-rate performances of all samples were investigated at various current densities of 1, 3,

5, 7, and 10 C (Fig. 6b), and the charging/discharging curves are shown in Fig. S2. While the specific capacity of the bare LMO electrode rapidly decreased from 107.9 mAh/g to 42.1 mAh/g with increasing C-rate, the NTO-LMO40 electrode showed a superior C-rate performance of 119.1–74.7 mAh/g than those of other NTO-LMO samples (94.8–57.1 mAh/g for NTO-LMO20 electrode and 101.9–65.4 mAh/g for NTO-LMO60 electrode) owing to the optimized NTO functional layer that provided a high electron/ion

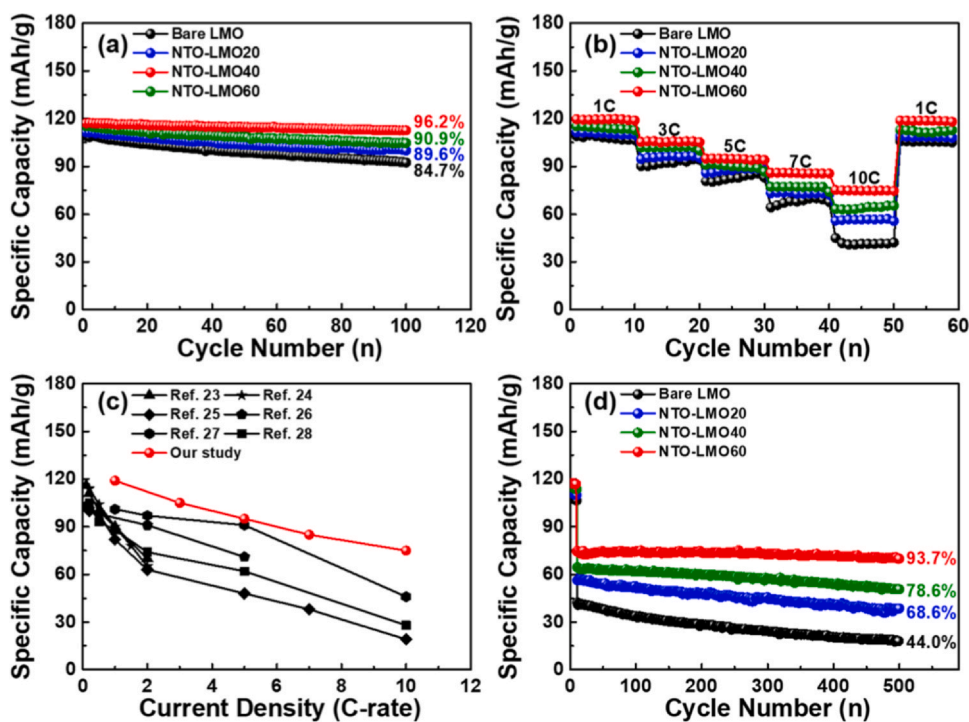


Fig. 6. (a) Cycling stability at current density of 1 C during 100 cycles, (b) comparison of rate-performance with formerly reported results of surface coated LMO cathode materials in the LIBs, (c) rate-performance at various current densities of 1 C, 3 C, 5 C, 7 C, 10 C, and 1 C, and (d) ultrafast cycling stability at 10 C during 500 cycles.

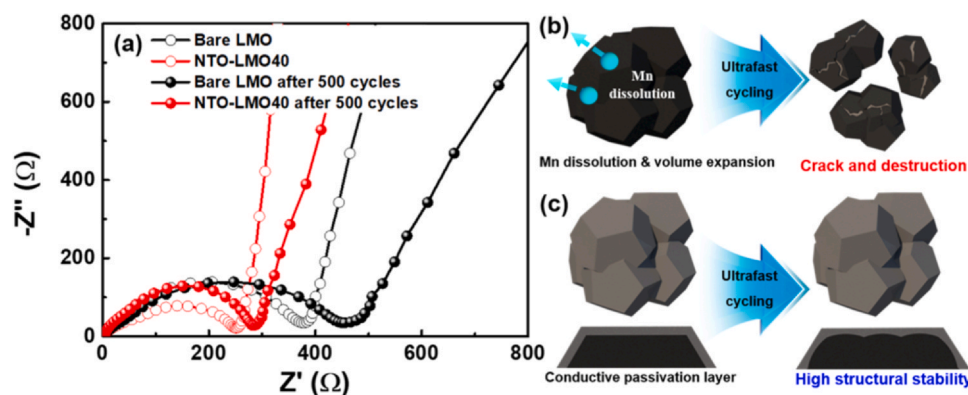


Fig. 7. (a) Nyquist plots of the bare LMO and NTO-LMO40 electrodes in the frequency range of 10^2 kHz– 10^{-2} Hz after 500 cycles measured at current density of 10 C, (b, c) the schematic illustration of electrochemical behavior of bare LMO and NTO-LMO40.

transfer rate. Also, as shown in Fig. S4, the rate performance of pure TiO_2 coated LMO electrode without Nb doping was demonstrated. The pure TiO_2 coated LMO electrode has relatively poor rate performance with capacity retention of 51.4% at increased current density from 1 C to 10 C compared to that of NTO-LMO40 electrode (62.7%), which can be attributed to low electrical/ionic conductivities of TiO_2 . Thus, the rate performance of NTO-LMO electrode at 10 C exhibits 1.35 times higher than that of pure TiO_2 -LMO due to Nb doping effect. Furthermore, NTO-LMO40 exhibited superior C-rate performance compared with those of other surface-coated LMO materials reported previously (Fig. 4c) [31–36]. And detail specific capacity at high C-rate of surface coated LMO materials reported previously is summarized at Table. S1. In addition, Fig. 4d shows the ultrafast cycling performance of all samples measured at 10 C for up to 500 cycles. Compared to those of other electrodes, the NTO-LMO40 electrode exhibited a superior ultrafast cycling capacity of 69.9 mAh/g with a capacity retention of 93.7% after 500 cycles. This is mainly attributed to the beneficial electrical/ionic conductivity of the NTO functional surface coating layer. To verify the effect of the conductive NTO functional coating layer on the LMO surface, the EIS analysis was performed using the cells in which the ultrafast cycling test was completed, as shown in Fig. 7a. The bare-LMO electrode showed high R_{ct} and Warburg impedance owing to structural destruction resulting from Mn dissolution and volume expansion of LMO, whereas the R_{ct} and Warburg impedance of the NTO-LMO40 electrode remained low even after the cycling test at a high C-rate of 10 C over 500 cycles, because of the effective suppression of Mn dissolution and prevention of volume expansion of LMO. Also, the cyclic voltammetry of bare LMO and NTO-LMO40 during 50 cycles at scan rate of 1 mV/s (as shown in Fig. S5) was performed, and the NTO-LMO40 electrode has reduced shift of redox peaks (+0.012 and -0.022 V) compared to that of bare LMO (+0.013 and -0.048 V), which implies the conductive NTO functional layer can effectively prevent Mn dissolution by Jahn-Teller distortion [21,37,38]. Furthermore, in the FESEM images of bare-LMO and NTO-LMO40 electrodes after 500 cycles at 10 C (see Fig. S6), NTO-LMO electrode shows maintained structure of primary LMO particles. Because the molar volume of the LMO is expanded by the inserted Li ions, the conductive NTO functional layer can physically buffer the change of molar volume. Therefore, while the bare-LMO structure were collapsed due to repetitive volume change, the NTO-LMO particles were maintained by physical buffer layer [39]. For the EDS results (Table. S2) of bare LMO and NTO-LMO40 after 500 cycles at 10 C, the NTO-LMO40 show reduced Mn dissolution (1.32 at%) compared to bare LMO (6.46 at%), which means that the conductive NTO functional layer can effectively prevent Mn dissolution after ultrafast cycling.

In general, the bare-LMO electrode undergoes extreme structural stress under ultrafast cycling conditions due to volume changes and Mn dissolution, leading to poor ultrafast cycling performance. In contrast, NTO-LMO40 exhibited remarkable ultrafast cycling performance because the conductive NTO functional layer effectively suppressed Mn dissolution and volume expansion of LMO (Fig. 7b). Thus, in this study, the improved electrochemical performance can be attributed to two main effects (as shown in Fig. 8): (1) the optimized interfacial layer of NTO prevented Mn dissolution and volume expansion during cycling, thus increasing the cycling stability; (2) the high electrical/ionic conductivity of NTO provided improved Li storage kinetics, thus enhancing the ultrafast cycling performance.

4. Conclusions

We fabricated an NTO functional layer on the surface of LMO using HUSPD. With optimization of the deposition time, NTO-LMO40 showed an outstanding specific capacity of 112.7 mAh/g with a high capacity retention of 96.2% after 100 cycles at a current density of 1 C and excellent ultrafast cycling capability of 70.0 mAh/g after 500 cycles at a current density of 10 C. This increased Li storage performance are attributed to the synergistic effect: (1) the enhanced cycling stability is related to the thin and dense NTO functional layer coated on the LMO surface, which can prevent Mn dissolution by Jahn-Teller distortion and can suppress volume expansion; (2) the exceptional ultrafast cycling performance is ascribed to doped Nb atoms into the TiO_2 structure, which can enhance the electrical conductivity and Li-ion diffusion rate by expanding the lattice distance of *c*-axis and increasing the electron concentration. Therefore, the conductive NTO coated LMO has a great potential as a high-performance cathode material for ultrafast LIBs.

CRediT authorship contribution statement

Ki-Wook Sung: Conceptualization, Methodology, Investigation, Writing - original draft. **Dong-Yo Shin:** Methodology, Writing - original draft. **Hyo-Jin Ahn:** Conceptualization, Supervision, Writing - review & editing.

Declaration of Competing Interest

The authors declare that they have no known competing financial interests or personal relationships that could have appeared to influence the work reported in this paper.

Conductive NTO coating layer on surface of LMO

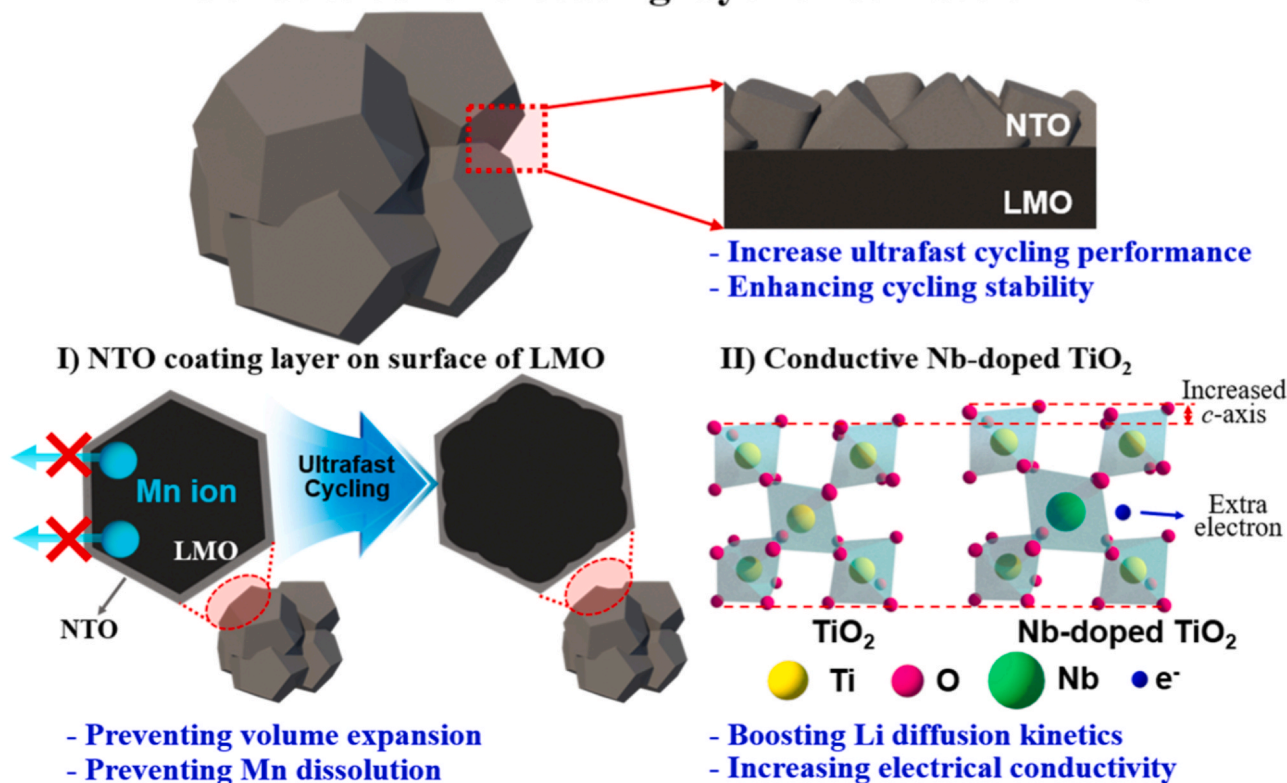


Fig. 8. The schematic illustration of the two main effect of the NTO-LMO40 electrode for enhancing ultrafast Li storage performances.

Acknowledgments

This work was supported by the National Research Foundation of Korea (NRF) grant funded by the Korea government (MSIT) (No. 2019R1 A2 C1005836).

Appendix A. Supporting information

Supplementary data associated with this article can be found in the online version at [doi:10.1016/j.jallcom.2021.159404](https://doi.org/10.1016/j.jallcom.2021.159404).

References

- [1] J.H. Ang, C. Goh, A.A.F. Saldívar, Y. Li, Energy-efficient through-life smart design, manufacturing and operation of ships in an industry 4.0 environment, *Energies* 10 (2017) 610.
- [2] M. Armand, J.-M. Tarascon, Building better batteries, *Nature* 451 (2008) 652–657.
- [3] P.G. Bruce, B. Scrosati, J.-M. Tarascon, Nanomaterials for rechargeable lithium batteries, *Angew. Chem. Int. Ed.* 47 (2008) 2930–2946.
- [4] B.-R. Koo, K.-W. Sung, H.-J. Ahn, Boosting ultrafast lithium storage capability of hierarchical core/shell constructed carbon nanofiber/3D interconnected hybrid network with nanocarbon and FTO nanoparticle heterostructures, *Adv. Funct. Mater.* 30 (2020) 1–11 2001863.
- [5] F. Zhang, T. Zhang, X. Yang, L. Zhang, K. Leng, Y. Huang, Y. Chen, A high-performance supercapacitor-battery hybrid energy storage device based on graphene-enhanced electrode materials with ultrahigh energy density, *Energy Environ. Sci.* 6 (2013) 1623–1632.
- [6] P.K. Nayak, L. Yang, W. Brehm, P. Adelhelm, From lithium-ion to sodium-ion batteries: advantages, challenges, and surprises, *Angew. Chem. Int. Ed.* 57 (2018) 102–120.
- [7] L. Lu, X. Han, J. Li, J. Hua, M. Ouyang, A review on the key issues for lithium-ion battery management in electric vehicles, *J. Power Sources* 226 (2013) 272–288.
- [8] Y.-K. Sun, Z. Chen, H.-J. Noh, D.-J. Lee, H.-G. Jung, Y. Ren, S. Wang, C. Yoon, S.-T. Myung, Y. Ren, Nanostructured high-energy cathode materials for advanced lithium batteries, *Nat. Mater.* 11 (2012) 942–947.
- [9] D.-Y. Shin, Y.-G. Lee, H.-J. Ahn, One-pot synthesis of aluminum oxide coating and aluminum doping on lithium manganese oxide nanoparticles for high performance energy storage system, *J. Alloy. Compd.* 727 (2017) 1165–1170.
- [10] K.M. Shaju, P.G. Bruce, A stoichiometric nano-LiMn₂O₄ spinel electrode exhibiting high power and stable cycling, *Chem. Mater.* 20 (2008) 5557–5562.
- [11] Y. Liu, X. Li, H. Guo, Z. Wang, Q. Hu, W. Peng, Y. Yang, Electrochemical performance and capacity fading reason of LiMn₂O₄/graphite batteries stored at room temperature, *J. Power Sources* 189 (2009) 712–725.
- [12] Y. Kim, J. Lim, S. Kang, Investigation on the dissolution of Mn ions from LiMn₂O₄ cathode in the application of lithium ion batteries: first principle molecular orbital method, *Int. J. Quantum Chem.* 113 (2013) 148–154.
- [13] H.-W. Ha, N.J. Yun, K. Kim, Improvement of electrochemical stability of LiMn₂O₄ by CeO₂ coating for lithium-ion batteries, *Electrochim. Acta* 52 (2007) 3236–3241.
- [14] D. Zhang, B.N. Popov, R.E. White, Electrochemical investigation of CrO_{2.65} doped LiMn₂O₄ as a cathode material for lithium-ion batteries, *J. Power Source* 76 (1998) 81–90.
- [15] S. Kuwabata, S. Masui, H. Yoneyama, Charge-discharge properties of composites of LiMn₂O₄ and polypyrrole as positive electrode materials for 4 V class of rechargeable Li batteries, *Electrochim. Acta* 44 (1999) 4593–4600.
- [16] Y. Lin, M.X. Gao, D. Zhu, Y.F. Liu, H.G. Pan, Effects of carbon coating and iron phosphides on the electrochemical properties of LiFePO₄/C, *J. Power Source* 184 (2008) 444–448.
- [17] J. Gao, T. Yuan, S. Luo, J. Ruan, H. Sun, H. Sun, J. Yang, S. Zheng, Boosting lithium ion storage of lithium nickel manganese oxide via conformally interfacial nano-coating, *J. Colloid Interface Sci.* 570 (2020) 153–162.
- [18] M. Fehse, S. Cavaliere, P.E. Lippens, I. Savych, A. Iadecola, L. Monoconduit, D.J. Jones, J. Roziere, F. Fischer, C. Tessier, L. Stievano, Nb-doped TiO₂ nanofibers for lithium ion batteries, *J. Phys. Chem. C* 117 (2013) 13827–13835.
- [19] H. Usui, S. Yoshioka, K. Wasada, M. Shimizu, H. Sakaguchi, Nb-doped rutile TiO₂: a potential anode material for Na-ion battery, *ACS Appl. Mater. Interfaces* 7 (2015) 6567–6573.
- [20] B.-R. Koo, D.-H. Oh, H.-J. Ahn, Improvement of transparent conducting performance on oxygen-activated fluorine-doped tin oxide electrodes formed by horizontal ultrasonic spray pyrolysis deposition, *ACS Appl. Mater. Interfaces* 9 (2017) 44584–44592.
- [21] D.-Y. Shin, B.-R. Koo, H.-J. Ahn, Lithium storage kinetics of highly conductive F-doped SnO₂ interfacial layer on lithium manganese oxide surface, *Appl. Surf. Sci.* 499 (2020) 144057144057–144055.

- [22] F. Zhao, B. Wang, Y. Tang, H. Ge, Z. Huang, H.K. Liu, Niobium doped anatase TiO₂ as an effective anode material for sodium-ion batteries, *J. Mater. Chem. A* 3 (2015) 22969–22974.
- [23] B. Mei, M.D. Sanchez, T. Reinecke, S. Kaluza, W. Xia, M. Muhler, The synthesis of Nb-doped TiO₂ nanoparticles by spray drying: an efficient and scalable method, *J. Mater. Chem.* 21 (2011) 11781–11790.
- [24] S. Tao, H. Zhao, C. Wu, H. Xie, P. Cui, T. Xiang, S. Chen, L. Zhang, Y. Fang, Z. Wang, W. Chu, B. Qian, L. Song, Enhanced electrochemical performance of MoO₃-coated LiMn₂O₄ cathode for rechargeable lithium-ion batteries, *Mater. Chem. Phys.* 199 (2017) 203–208.
- [25] B.-R. Koo, D.-H. Oh, H.-J. Ahn, Influence of Nb-doped TiO₂ blocking layers as a cascading band structure for enhanced photovoltaic properties, *Appl. Surf. Sci.* 433 (2018) 27–34.
- [26] M. Lubke, J. Shin, P. Marchand, D. Brett, P. Shearing, Z. Liu, J.A. Darr, Highly pseudocapacitive Nb-doped TiO₂ high power anodes for lithium-ion batteries, *J. Mater. Chem. A* 3 (2015) 22908–22914.
- [27] M. Kwoka, V. Galstyan, E. Comini, J. Szuber, Pure and highly Nb-doped titanium dioxide nanotubular arrays: characterization of local surface properties, *Nanomaterials* 7 (2017) 456–458.
- [28] X. Han, K. Song, L. Lu, Q. Deng, X. Xia, G. Shao, Limitation and extrapolation correction of the GGA + U formalism: a case study of Nb-doped anatase TiO₂, *J. Mater. Chem. C* 1 (2013) 3736–3746.
- [29] K.-W. Sung, B.-R. Koo, H.-J. Ahn, Hybrid nanocomposites of tunneled-mesoporous sulfur-doped carbon nanofibers embedded with zinc sulfide nanoparticles for ultrafast lithium storage capability, *J. Alloy. Compd.* 854 (2021) 157206–157206–157105.
- [30] K.-W. Sung, H.-J. Ahn, Titanium dioxide nanoparticles dispersed in heteroatom-doped carbon nanofibers for ultrafast lithium storage, *J. Ceram. Process. Res.* 21 (2020) 1–9.
- [31] S. Zhao, Y. Bai, L. Ding, B. Wang, W. Zhang, Enhanced cycling stability and thermal stability of YPO₄-coated LiMn₂O₄ cathode materials for lithium ion batteries, *Solid State Ion.* 247 (2018) 22–29.
- [32] A.M. Hashem, A.E. Abdel-Ghany, H.N. Abuzeid, R.S. El-Tawil, S. Indris, H. Ehrenberg, A. Mauger, C.M. Julien, EDTA as chelating agent for sol-gel synthesis of spinel LiMn₂O₄ cathode material for lithium batteries, *J. Alloy. Compd.* 737 (2018) 758–766.
- [33] S. Zhao, Y. Bai, Q. Chang, Y. Yang, W. Zhnag, Surface modification of spinel LiMn₂O₄ with FeF₃ for lithium ion batteries, *Electrochim. Acta* 108 (2013) 727–735.
- [34] A. Tron, Y.D. Park, J. Mun, AlF₃-coated LiMn₂O₄ as cathode material for aqueous rechargeable lithium battery with improved cycling stability, *J. Power Sources* 325 (2016) 360–364.
- [35] J. Zeng, M. Li, X. Li, C. Chen, D. Xiong, L. Dong, D. Li, A. Lushington, X. Sun, A novel coating onto LiMn₂O₄ cathode with increased lithium ion battery performance, *Appl. Surf. Sci.* 217 (2014) 884–891.
- [36] Y. Shang, X. Lin, X. Lu, T. Huang, A. Yu, Nano-TiO₂(B) coated LiMn₂O₄ as cathode materials for lithium-ion batteries at elevated temperatures, *Electrochim. Acta* 156 (2015) 121–126.
- [37] K.Y. Chung, C.W. Ryu, K.B. Kim, Onset mechanism of Jahn-Teller distortion in 4 V LiMn₂O₄ and its suppression by LiM_{0.05}Mn_{1.95}O₄ (M = Co, Ni) coating, *J. Electrochem. Soc.* 152 (2005) A791–A795.
- [38] N. Ohta, K. Takada, L. Zhang, R. Ma, M. Osada, T. Sasaki, Enhancement of the highrate capability of solid-state lithium batteries by nanoscale interfacial modification, *Adv. Mater.* 18 (2006) 2226–2229.
- [39] R. Koerver, W. Zhang, L.D. Biasi, S. Schweidler, A.O. Kondrakov, S. Kolling, T. Brezesinski, P. Hartmann, W.G. Zeier, J. Janek, Chemo-mechanical expansion of lithium electrode materials – on the route to mechanically optimized all-solid-state batteries, *Energy Environ. Sci.* 11 (2018) 2142–2158.